PHYSICAL REVIEW B **107**, 075124 (2023)

Node-line Dirac semimetal manipulated via Kondo mechanism in nonsymmorphic $CePt_2Si_2$

Hao-Tian Ma,[1] Xing Ming,[1] Xiao-Jun Zheng,[1] Jian-Feng Wen,[1] Yue-Chao Wang,[2] Yu Liu,[2] and Huan Li[1,*]
[1]*College of Science, Guilin University of Technology, Guilin 541004, China*
[2]*Laboratory of Computational Physics, Institute of Applied Physics and Computational Mathematics, Beijing 100088, China*

(Received 6 December 2022; accepted 30 January 2023; published 9 February 2023)

Dirac node lines (DNLs) are characterized by Dirac-type linear crossings between valence and conduction bands along one-dimensional node lines in the Brillouin zone (BZ). Spin-orbit coupling (SOC) usually shifts the degeneracy at the crossings thus destroys DNLs, and so far the reported DNLs in a few materials are noninteracting type, making the search for robust interacting DNLs in real materials appealing. Here, via first-principle calculations, we reveal that Kondo interaction together with nonsymmorphic lattice symmetries can drive a robust interacting DNLs in a Kondo semimetal $CePt_2Si_2$, and the feature of DNLs can be significantly manipulated by Kondo behavior in different temperature regions. Based on the density functional theory combining with dynamical mean-field theory (DFT + DMFT), we predict a transition to Kondo-coherent state at coherent temperature $T_{\rm coh} \approx 80$ K upon cooling, verified by temperature dependence of Ce-4f self-energy, Kondo resonance peak, magnetic susceptibility, and momentum-resolved spectral function. Below $T_{\rm coh}$, well-resolved narrow heavy-fermion bands emerge near the Fermi level, constructing clearly visualized interacting DNLs locating at the BZ boundary, in which the Dirac fermions have strongly enhanced effective mass and reduced velocity. In contrast, above a crossover temperature $T_{\rm KS} \approx 600$ K, the destruction of local Kondo screening drives noninteracting DNLs, which are comprised by light conduction electrons at the same location. These DNLs are protected by lattice nonsymmorphic symmetries thus robust under intrinsic strong SOC. Our proposal of DNLs, which can be significantly manipulated according to Kondo behavior provides an unique realization of interacting Dirac semimetals in real strongly correlated materials, and serves as a convenient platform to investigate the effect of electronic correlations on topological materials.

DOI: 10.1103/PhysRevB.107.075124

I. INTRODUCTION

Dirac semimetals, such as Na_3Bi [1] and Cd_3As_2 [2], are characterized by linear crossings between valence and conduction bands in momentum space, forming fourfold degenerate Dirac points describing by Dirac equation, and can be viewed as three-dimensional (3D) analogy of the two-dimensional (2D) Dirac points in graphene. By breaking of either time-reversal or space-inversion symmetry, individual Dirac point can be divided into a pair of Weyl points with opposite chiralities, as observed in TaAs [3] and Ag_2S [4], etc. In some materials with negligible spin-orbital coupling (SOC), the valence and conduction bands meet along a curved line or closed loop in the Brillouin zone, forming Dirac node lines (DNLs), which are usually unstable under action of SOC. Recently, DNLs in materials with space group Nos. 129 and 125 are proposed and confirmed by angle-resolved photoemission spectrums (ARPES) observations. In these materials such as ZrSiS [5–7] and $PtPb_4$ [8], the DNLs are protected by nonsymmorphic symmetries in their lattice space group, making them robust under SOC. Additionally, the Dirac fermions on these DNLs exhibit 2D character in momentum space [9].

In contrast to ZrSiS and $PtPb_4$, in which the electronic correlations are negligible, strong correlations may bring dramatic affects to the DNLs. As in the case of Weyl-Kondo semimetal $Ce_3Bi_4Pt_3$ [10,11], the strong correlation and Kondo hybridization result in renormalized Weyl fermions with highly enhanced effective mass and suppressed Fermi velocity, leading to characteristic T^3 dependence of specific heat [10], more remarkably, the correlations can give rise to nonlinear response behaviors such as giant spontaneous Hall effect [12,13]. Similarly, the electron correlations in material with DNLs may also induce notable affects to the Dirac fermions and arouse anomalous transport phenomena, which can be explored in future experiments; nevertheless, such interacting DNLs yet seem lack reporting in the literature.

In this article, we systematically explore nonsymmorphic Kondo semimetals $CePt_2Si_2$ and $CePt_2Ge_2$ by density functional theory combing with dynamical mean-field theory (DFT + DMFT). Firstly, we find that below a characteristic Kondo coherence temperature at about 80 K, $CePt_2Si_2$ becomes Kondo-coherent, forming interacting DNLs by heavy quasiparticles composed of conduction *spd* electrons and Ce-4f electrons. Secondly, above another crossover temperature at about 600 K, the local Kondo screening in $CePt_2Si_2$ has been destructed, hence the DNLs become noninteracting, consisting of only light conduction electrons. Due to larger unit cell volume, the DNLs in $CePt_2Ge_2$ remains noninteracting in all calculated temperature region. DNLs are also reported in a few rare-earth compounds such as centrosymmetric CeRhSb and CeNiSn [14], however, the correlated 4f electrons in

---

[*] lihuan@glut.edu.cn

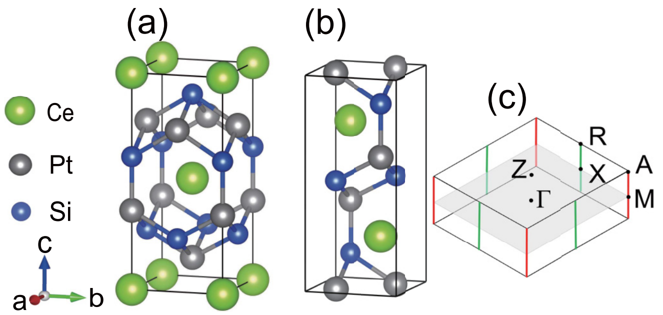

FIG. 1. (a) Primitive unit cell of $CePt_2Si_2$ with tetragonal $CaBa_2Ge_2$ type structure. (b) Equivalent unit cell displaying inversion and nonsymmorphic symmetries. (c) Corresponding Brillouin zone, in which the red and green lines denote the DNLs along M-A and X-R paths, respectively.

those materials are already localized thus their DNLs are actually created by conduction electrons only. In this context, to the best of our knowledge, $CePt_2Si_2$ is a suitable material with interacting DNLs in real strongly correlated materials.

The rest of this paper is arranged as follows. In Sec. II, we will analyze the crystal structures of $CePt_2Si_2$ and $CePt_2Ge_2$, and introduce the technical details of DFT + DMFT simulations in present paper. In Sec. III, we will present the DFT + DMFT results of $CePt_2Si_2$. Through synthetically analyses of self-energy, density of state, momentum-resolved spectral function, and the magnetic susceptibility, we will evaluate the two characteristic temperatures, firstly the Kondo coherent temperature driving the formation of coherent heavy-fermion hybridization bands, secondly the Kondo screening temperature below which the local Kondo screening of $4f$ electrons by conduction electrons turns on. In Sec. IV, we will discuss the emergence of interacting DNLs in $CePt_2Si_2$ below Kondo-coherent temperature, and also the noninteracting DNLs above the Kondo screening temperature. We will also verify the noninteracting DNLs in $CePt_2Ge_2$ based on its DFT and DFT + DMFT results. The last section Sec. V will give a brief discussion and conclusions.

II. CRYSTAL STRUCTURE AND COMPUTATIONAL METHOD

The primitive unit cell of $CePt_2Si_2$ is illustrated in Fig. 1(a), which crystalizes in the tetragonal $CaBa_2Ge_2$ type structure with space group $P4/nmm$ (No. 129). The lattice constants and atom positions of $CePt_2Si_2$ and isostructural $CePt_2Ge_2$ are collected in Table I according to Ref. [15]. From an alternate set of unit cell of $CePt_2Si_2$ in Fig. 1(b), the space inversion symmetry can be clearly seen. Besides the inversion symmetry, $CePt_2Si_2$ and $CePt_2Ge_2$ exhibit nonsymmorphic symmetries combining point group with fractional translation operations, namely the gliding mirror plane $\{M_z|\frac{1}{2},\frac{1}{2}\}$ and screw axes $\{C_{2x}|\frac{1}{2},0\}$, $\{C_{2y}|0,\frac{1}{2}\}$, where the origin of axes locate at the center of the unit cell in Fig. 1(b). $CePt_2Si_2$ was found to remain paramagnetic as low as 0.06 K [16], signaling the preservation of time-reversal symmetry. The nonsymmorphic symmetries combining time-reversal and inversion symmetries protect the fourfold degeneracy at X and

TABLE I. Crystal parameters of $CePt_2Si_2$ and $CePt_2Ge_2$ [15], the atomic positions correspond to Fig. 1(b).

	Lattice parameters	Ce position	Pt position	Si/Ge position
$CePt_2Si_2$	a = b = 4.252 Å	Ce(2c): $(\frac{1}{4},\frac{1}{4},0.7452)$, $(\frac{3}{4},\frac{3}{4},0.2548)$	Pt(2c): $(\frac{1}{4},\frac{1}{4},0.3798)$, $(\frac{3}{4},\frac{3}{4},0.6202)$	Si(2c): $(\frac{1}{4},\frac{1}{4},0.1329)$, $(\frac{3}{4},\frac{3}{4},0.8671)$
	c = 9.788 Å		Pt(2a): $(\frac{1}{4},\frac{3}{4},0)$, $(\frac{3}{4},\frac{1}{4},0)$	Si(2b): $(\frac{1}{4},\frac{3}{4},\frac{1}{2})$, $(\frac{3}{4},\frac{1}{4},\frac{1}{2})$
$CePt_2Ge_2$	a = b = 4.397 Å	Ce(2c): $(\frac{1}{4},\frac{1}{4},0.74)$, $(\frac{3}{4},\frac{3}{4},0.26)$	Pt(2c): $(\frac{1}{4},\frac{1}{4},0.383)$, $(\frac{3}{4},\frac{3}{4},0.617)$	Ge(2c): $(\frac{1}{4},\frac{1}{4},0.131)$, $(\frac{3}{4},\frac{3}{4},0.869)$
	c = 9.802 Å		Pt(2a): $(\frac{1}{4},\frac{3}{4},0)$, $(\frac{3}{4},\frac{1}{4},0)$	Ge(2b): $(\frac{1}{4},\frac{3}{4},\frac{1}{2})$, $(\frac{3}{4},\frac{1}{4},\frac{1}{2})$

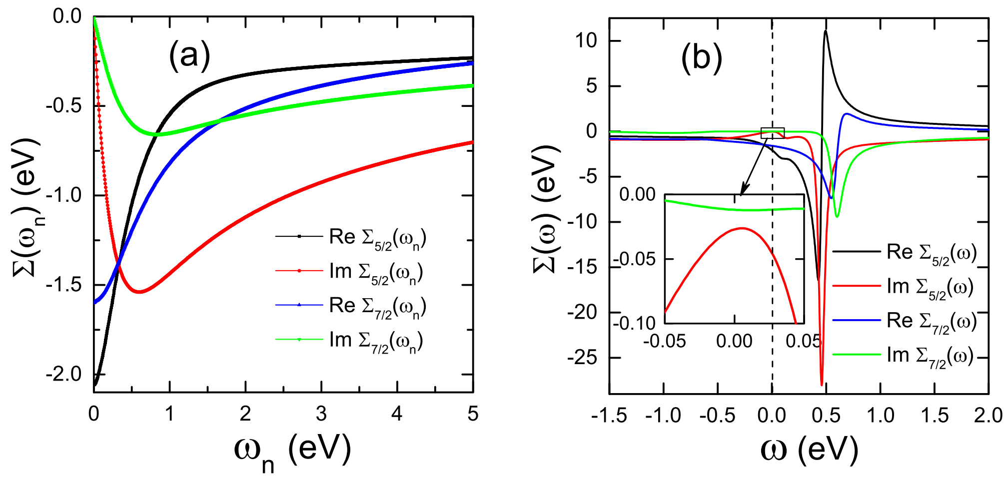

FIG. 2. Self-energies of $4f_{5/2}$ and $4f_{7/2}$ states via DFT + DMFT calculations of $CePt_2Si_2$ at 10 K on (a) imaginary-frequency axis and (b) real-frequency axis. Inset of (b) shows the detail near zero frequency.

M, and also along X-R and M-A lines in the Brillouin zone, creating the DNLs shown in Fig. 1(c), as will be discussed in detail below.

In order to explore the electron-correlation effects in $CePt_2Si_2$ and $CePt_2Ge_2$, we employ the density functional theory combined with dynamical mean-field theory (DFT + DMFT) embodied in the EDMFT package [17]. In each DFT + DMFT step, the DFT part implemented by full-potential linear augmented plane-wave method built in WIEN2k code [18] generates a single-particle Kohn-Sham Hamiltonian $\hat{H}_{\mathrm{KS}}$, then it is combined with an interacting term $\hat{H}_{\mathrm{int}}$ for Ce-$4f$ orbits and a double-counting term Σ_{dc} for self-energy, since DFT has already contained some form of electron correlations, and the resulting lattice model

$$\hat{H}_{\mathrm{DFT+DMFT}} = \hat{H}_{\mathrm{KS}} + \hat{H}_{\mathrm{int}} - \Sigma_{\mathrm{dc}} \tag{1}$$

is solved with single-site DMFT algorithm. In order to better fit experimental observations, we employ the on-site Coulomb repulsion $U = 5.0$ eV and Hund's coupling $J_H = 0.76$ eV on Ce-$4f$ orbits, similar to the value used in Refs. [19] and [14]. For Σ_{dc}, we use nominal double-counting,

$$\Sigma_{\mathrm{dc}} = U(n_f - 1/2) - J/2(n_f - 1), \tag{2}$$

where n_f is Ce-$4f$ occupancy. The DFT + DMFT calculations are executed iteratively to reach full-charge self consistence. Such DFT + DMFT method has been successfully applied in studying electronic correlations in a variety of materials, especially in rear-earth compounds [14,19–23].

In the DFT part, we use a $16 \times 16 \times 7$ k-mesh in the Brillouin zone integration, with a cut-off parameter K_{max} given by $R_{\mathrm{MT}}K_{\mathrm{max}} = 7.0$, and SOC is included throughout the calculations. The DFT band structures are also cross checked by VASP code. Each DFT + DMFT step contains one-shot DMFT and 20 steps of DFT calculations. The states within energy window [–10 eV, 10 eV] from the Fermi level are projected into the Anderson impurity problems. We use the hybridization expansion version of continuous-time quantum Monte Carlo method (CT-QMC) to solve the Anderson impurity problems, then perform analytical continuation by maximum-entropy method to obtain the real-frequency self-energies for f electrons. CT-QMC may be the most used impurity solver and has been employed down to very low temperature [11]. In each CT-QMC computation, 128 CPU cores are used to run $(5 \sim 30) \times 10^8$ QMC steps from 1000 K to 10 K. Typically, within $30 \sim 40$ DFT + DMFT iterations, full-charge self consistence can be reached, then we run additional five iterations to further average the self-energies. Since no magnetic order was found in $CePt_2Si_2$ and $CePt_2Ge_2$ down to 60 mK [16], we focus on the paramagnetic phase. In the impurity solver, the crystal-field splitting of f orbits has been examined and is found to be one more orders of magnitude smaller than the SOC splitting, hence the crystal-field splitting is neglected in present calculations. The SOC splits Ce-$4f$ orbits into $j = 5/2$ and $j = 7/2$ states, denoted by $4f_{5/2}$ and $4f_{7/2}$ respectively in the following.

III. CORRELATION EFFECT AND KONDO BEHAVIOR

In DFT + DMFT formulations, the electron correlation manifests itself following the local self-energies of f states. In Fig. 2, we plot the calculated DFT + DMFT local self-energies $\Sigma(\omega_n)$ and $\Sigma(\omega)$ for $CePt_2Si_2$ at temperature $T = 10\,\mathrm{K}$, on imaginary- and real-frequency axes respectively, where Matsubara frequency $\omega_n = (2n+1)\pi T$. In Fig. 2(a), the imaginary-part self-energies for both $4f_{5/2}$ and $4f_{7/2}$ states nicely approach zero at zero imaginary frequency, indicating Fermi-liquid-like character. The slope of imaginary-part self-energy $\mathrm{Im}\,\Sigma_{5/2}(\omega_n)$ for $4f_{5/2}$ state at zero frequency is about –9.3, which gives the quasiparticle spectral weight and mass enhancement factor

$$Z = 1/\left(1 - \frac{\partial \mathrm{Im}\,\Sigma_{5/2}(\omega_n)}{\partial \omega_n}|_{\omega_n \to 0^+}\right) = 0.097,$$
$$m^*/m_{DFT} = 1/Z = 10.3, \tag{3}$$

respectively, it means that the band width of $4f_{5/2}$ bands is strongly reduced to be roughly ten times narrow than in DFT, as will be verified in the following. Large value of m^*/m_{DFT} is the origin of large specific heat of $CePt_2Si_2$ observed at low temperature [24]. The self-energies on real axis are created through analytical continuation of $\Sigma(\omega_n)$ by maximum entropy method, and are shown in Fig. 2(b). The real-part self-energies for both $4f_{5/2}$ and $4f_{7/2}$ states show rapid variations

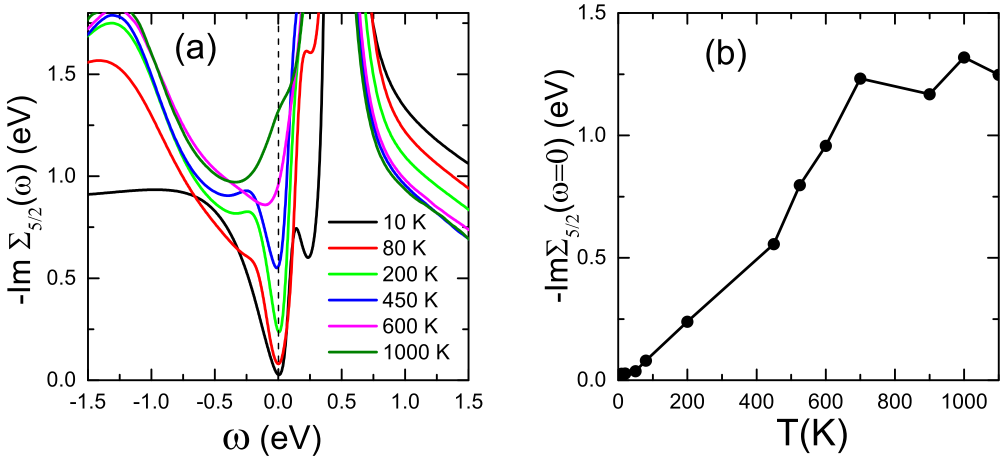

FIG. 3. (a) Imaginary part of $4f_{5/2}$ self-energy $\text{Im}\Sigma_{5/2}(\omega)$ vs ω at different temperatures. (b) Evolution of $-\text{Im}\Sigma_{5/2}(\omega = 0)$ with temperature.

between $\omega = (0.2\text{ eV}, 1\text{ eV})$, leading to significant modifies of f bands from DFT results by correlations, as will be seen below. At $T = 10\,\text{K}$, the imaginary self-energy $\text{Im}\Sigma_{5/2}(\omega)$ of $4f_{5/2}$ state has a small value 27.2 meV at $\omega = 0$, gives rise to low-scattering rate and relatively long lift time for quasiparticles at the Fermi level.

Figure 3(a) demonstrates the evolution of imaginary self-energy $\text{Im}\Sigma_{5/2}(\omega)$ for $4f_{5/2}$ state as a function of frequency ω, at various temperatures. Below 80 K, a clear and sharp dip near $\omega = 0$ appears, reaching a quite small value at the bottom. Such dip of $\text{Im}\Sigma_{5/2}(\omega)$ near $\omega = 0$ will directly drive an intense Kondo resonance peak in the $4f_{5/2}$ density of states (DOS) (see below), and can be interpreted as the onset of Kondo coherence [19,21] below a characteristic coherent temperature $T_{\text{coh}} \approx 80\,\text{K}$. Moreover, the sharp dip of $\text{Im}\Sigma_{5/2}(\omega)$ below T_{coh} also induces clearly resolved $4f$ bands, further verifying the Kondo coherence below T_{coh}, as will be discussed below. Besides, below 80 K, $\text{Im}\Sigma_{5/2}(\omega)$ can be well fitted by a parabolic function $\text{Im}\Sigma_{5/2}(\omega) \approx -\alpha(\omega - \omega_0)^2 - \Sigma_0$, with $\alpha = 29.7\,\text{eV}^{-1}$, $\omega_0 = 5\,\text{meV}$, $\Sigma_0 = 26.5\,\text{meV}$ at 10 K, also suggesting Fermi-liquid behavior at low temperature, in accordance with the interpretation from resistivity and specific heat experiments [24,25]. As temperature rises, the dip of $\text{Im}\Sigma_{5/2}(\omega)$ is suppressed gradually, while above 600 K, the narrow dip starts to vanish, leaving a broad minimum considerably away from $\omega = 0$, resulting in a greatly weakened $4f$ DOS. In Fig. 3(b), the magnitude of $-\text{Im}\Sigma_{5/2}(\omega = 0)$ is plotted as temperature varies. Below 10 K, $-\text{Im}\Sigma_{5/2}(0)$ tends to be saturated and approaches about 27 meV at zero temperature, while temperature rises, it shows a gradually increase, then turns to stay around a large magnitude of 1.25 eV at $T >$600 K, which makes $4f$ electrons localized at high temperature, as will be further clarified below. The many-body Kondo screening of local $4f$ electrons by conduction electrons creates an enormous enhancement in the DOS of Ce-$4f$ states near the Fermi level, i.e., the Kondo resonance peak. In Fig. 4(a), the total and $4f$ DOS of CePt$_2$Si$_2$ are plotted as functions of energy, from 10 K to 1000 K, displaying significant difference near the Fermi level as temperature rises. At low temperatures (see 10 K and 80 K cases), two narrow peaks (peak width about 20 meV) dominated by $4f$ states appear with large height, in which the one contributed by $4f_{5/2}$ state centers at 14 meV above the Fermi level with its tail crosses E_F, the other owning to $4f_{7/2}$ state locates at 0.351 eV above E_F, and the corresponding SOC splitting between these two peaks is about 0.337 eV, as shown in Fig. 4(b). As temperature increases, the two resonance peaks decrease considerably but are still visible up to 1000 K, owning to relatively strong impurity hybridization function in DFT + DMFT calculation, which indicates a strong c-f hybridization in CePt$_2$Si$_2$ in wide temperature range.

Since the Kondo resonance peak is dominated by the low-lying $4f_{5/2}$ state, we plot the evolution of its peak height with temperature in Fig. 4(c). The Kondo resonance peak carries large height at low temperatures and shows a saturation tendency below 10 K, which arises from similar saturation behavior of $-\text{Im}\Sigma_{5/2}(0)$ in Fig. 3(b). As temperature rises from 10 K, the peak height first drops rapidly, then turns to decrease much slowly, and eventually varies smoothly to maintain a small magnitude above 600 K. Below 80 K, the Kondo coherence sets in and manifests itself by a rapid increase of resonance peak, further confirming the appearance of Kondo coherence below coherent temperature $T_{\text{coh}} \approx 80\,\text{K}$. While above 600 K, Kondo resonance peak is greatly reduced, and only accounts for a small proportion in the total DOS, indicating that the $4f$ electrons are already localized to form local moments, similar to the $4f$ states in CeSb, CeIrIn5 and CeIn3 in their local-moment regions [19,20,26]. Therefore, we obtain another characteristic Kondo-screening temperature $T_{\text{KS}} \approx 600\,\text{K}$, below which the conduction *spd* electrons start to screen the localized Ce-$4f$ electrons to form Kondo singlet states, and consequently generate Kondo resonance peak gradually in $4f$ DOS near the Fermi level. Apart from the resonance peaks, the on-site Coulomb repulsion between $4f$ electrons also produces broad lower and upper Hubbard bands in the $4f$ DOS, concentrated mainly between (–3 eV, –1 eV) and (1.5 eV, 4 eV) from the Fermi level, respectively, and the distance between their centers is roughly 4.3 eV, comparable with Hubbard strength $U = 5\,\text{eV}$. Besides, there is very little DOS weight in the lower Hubbard band thus hard to identify, while the upper Hubbard band has large intensity in the DOS. The probabilities of Ce-$4f$ atomic states are calculated via

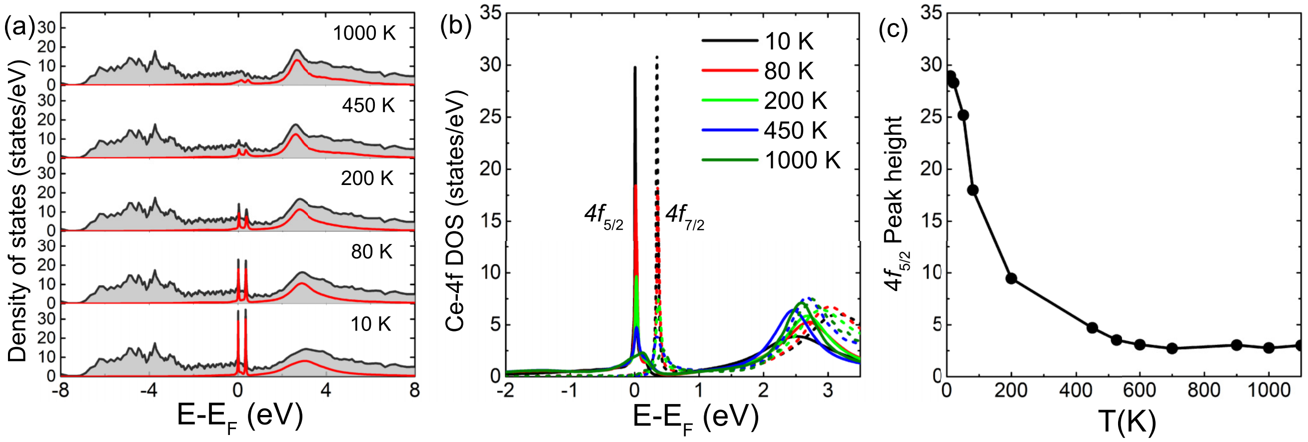

FIG. 4. (a) Density of states (DOS) of $\mathrm{CePt_2Si_2}$ from temperature 10 K to 1000 K via DFT + DMFT calculations. The black-solid lines denote total DOS, and the red lines denote Ce-$4f$ DOS. The paired $4f$ peaks become more and more prominent as temperature drops. (b) Projected Ce-$4f$ DOS at different temperatures. The solid lines denote $4f_{5/2}$ DOS, while the dashed lines denote $4f_{7/2}$ DOS. The splitting of $4f$ DOS is caused by SOC. (c) Temperature variation of $4f_{5/2}$ peak height, implying formation of local Kondo screening and Kondo resonance below $T_{\mathrm{KS}} \approx 600\,\mathrm{K}$.

CT-QMC solver. At 10 K, $4f^0$, $4f^1$, $4f^2$, and $4f^3$ configurations account for probabilities of 0.06167, 0.86129, 0.0729, and 0.0013, respectively, indicating the dominance by $4f^1$ state, and resulting in $4f$ occupance $n_f = 1.017$, which varies very weakly with temperature.

We now turn to the magnetic susceptibility of $\mathrm{CePt_2Si_2}$. In Fig. 5, the local spin susceptibility χ_s and its inverse χ_s^{-1} are illustrated as functions of temperature, computed by CT-QMC solver in DFT + DMFT iterations. In Fig. 5(a), χ_s shows a faster increase upon cooling, then undergoes an abrupt decrease below 80 K. At $T > 80\,\mathrm{K}$, χ_s can be well fitted by the Curie-Weiss form $\chi_s = C/(T+\theta)$ with $\theta \approx 92\,\mathrm{K}$, and starts to deviate from the Curie-Weiss formula considerably below 80 K. Such temperature dependence of magnetic susceptibility shows consistence with experimental results [24,25,27], and provides strong evidence of the appearance of Kondo coherence below coherence temperature $T_{\mathrm{coh}} = 80\,\mathrm{K}$, similar to Kondo semimetal $\mathrm{CeFe_2Al_{10}}$ [28].

The above analyses of $4f$ self-energies, Kondo resonance peak and magnetic susceptibility clearly witness a Kondo mechanism of $\mathrm{CePt_2Si_2}$. Above a crossover temperature $T_{\mathrm{KS}} \approx 600\,\mathrm{K}$, the Ce-$4f$ electrons are tightly bound and fully localized inside Ce atoms, thus are totally decoupled from itinerant electrons to form local moments. Reduction of temperature from T_{KS} induces local Kondo screening of local moments by conduction electrons gradually, results in Kondo singlet states and arouses Kondo resonance peak near the Fermi level. Further cooling to below $T_{\mathrm{coh}} \approx 80\,\mathrm{K}$ drives indirect nonlocal Ruderman-Kittel-Kasuya-Yosida (RKKY) interaction between f electrons [29], which creates a Kondo-coherent many-body state and gives rise to intense Kondo resonance peak and well-resolved heavy-fermion hybridization bands.

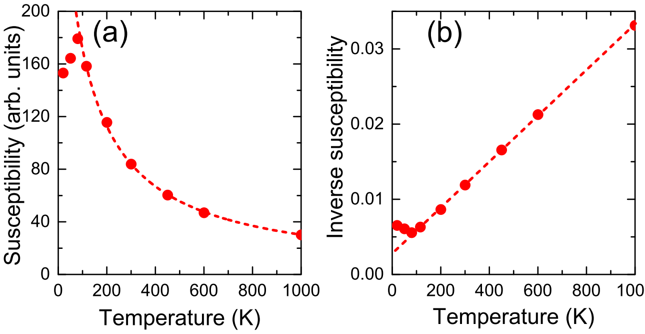

FIG. 5. Red dots show the temperature dependence of (a) local magnetic susceptibility χ_s and (b) inverse susceptibility χ_s^{-1} for $\mathrm{CePt_2Si_2}$, via DFT + DMFT calculations. For comparison, the Curis-Weiss form $\chi_s = C/(T+\theta)$ is denoted by red-dashed lines.

IV. THE DIRAC NODE LINES

The transition to Kondo coherent state below T_{coh} can be witnessed by temperature variation of spectral function, which can be measured directly via ARPES experiments. In Fig. 6, the momentum-resolved spectral function $A(\mathbf{k}, \omega)$ of $\mathrm{CePt_2Si_2}$ calculated by DFT + DMFT is plotted along a representative high-symmetry path in the Brillouin zone, in temperature range from 10 K to 1000 K. Below 80 K, the intense spectral weight of two groups of weakly dispersive heavy-fermion bands, which concentrate near 14 meV and 0.351 eV above the Fermi level, respectively, can be clearly seen, through which the two narrow resonance peaks in DOS [Fig. 4(a)] can be directly obtained via $\rho(\omega) = \sum_{\mathbf{k}} A(\mathbf{k}, \omega)$. The sharply resolved heavy-fermion bands near the Fermi level below 80 K again verifies formation of Kondo coherence below $T_{\mathrm{coh}} \approx 80\,\mathrm{K}$. As temperature rises from T_{coh}, the hybridization bands become more and more blurred and are no longer well resolved.

Above the local Kondo screening temperature $T_{\mathrm{KS}} \approx 600\,\mathrm{K}$, the intensity of hybridization bands is dramatically diminished [see Fig. 6(e) at 1000 K], leading to low $4f$ DOS peaks [see the top pattern in Fig. 4(a)], consequently the $4f$ electrons are fully localized, and the bands near the Fermi level become highly dispersive, see Fig. 6(j). Figure 7(c) shows the DFT bands treating $4f$ orbits as open-core states

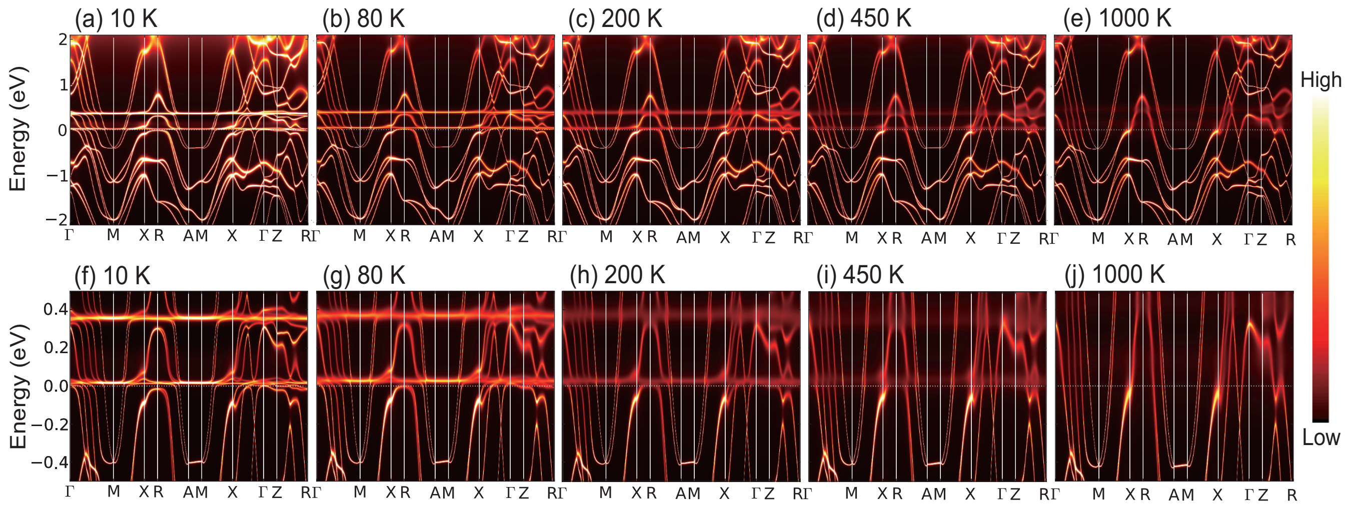

FIG. 6. DFT + DMFT momentum-resolved spectral function of $CePt_2Si_2$ from 10 K to 1000 K. The bottom patterns are just zoomed-in view of top patterns. From 10 K to 80 K, the hybridization bands near the Fermi level are clearly resolved, while at 1000 K, the hybridization bands are already blurred out, leaving highly-dispersive conduction bands and signaling local-moment nature of Ce-4f electrons at high temperature.

[30], which can nicely reproduce high-temperature DFT + DMFT result in Fig. 6(e), further confirming the local moment nature of 4f states at $T > T_{KS}$. It should be noted that the spectral weight of 4f electrons remains nonvanished even at $T > T_{KS}$, similar to γ-Ce, CeSb, and $CeIn_3$ in their local-moment regions [20,21,26].

The clearly distinguished DFT + DMFT hybridization bands at 10 K are illustrated in Fig. 6(f) and enlarged in

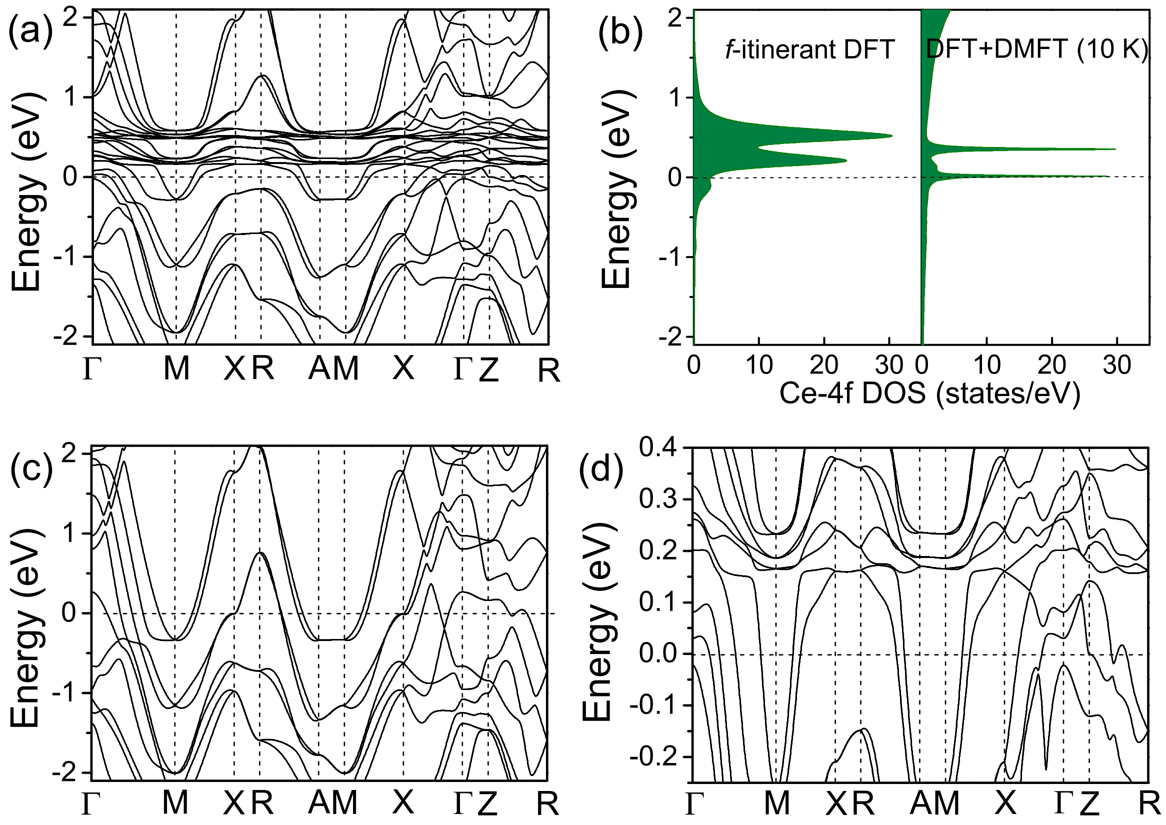

FIG. 7. DFT bands of $CePt_2Si_2$ treating Ce-4f electrons as (a) itinerant and (c) open-core states. (d) is just a zoomed-in view of (a) near the Fermi level. The bands are degenerate at X, R, M, A and along X-R and M-A paths, leading to DNLs locating on X-R and M-A lines shown in Fig. 1(c). Ce-4f bands in (a) are divided into $4f_{5/2}$ and $4f_{7/2}$ bands under SOC splitting, contributing double 4f DOS peaks in (b), by comparison, DFT + DMFT leads to much narrow 4f DOS peaks at 10 K.

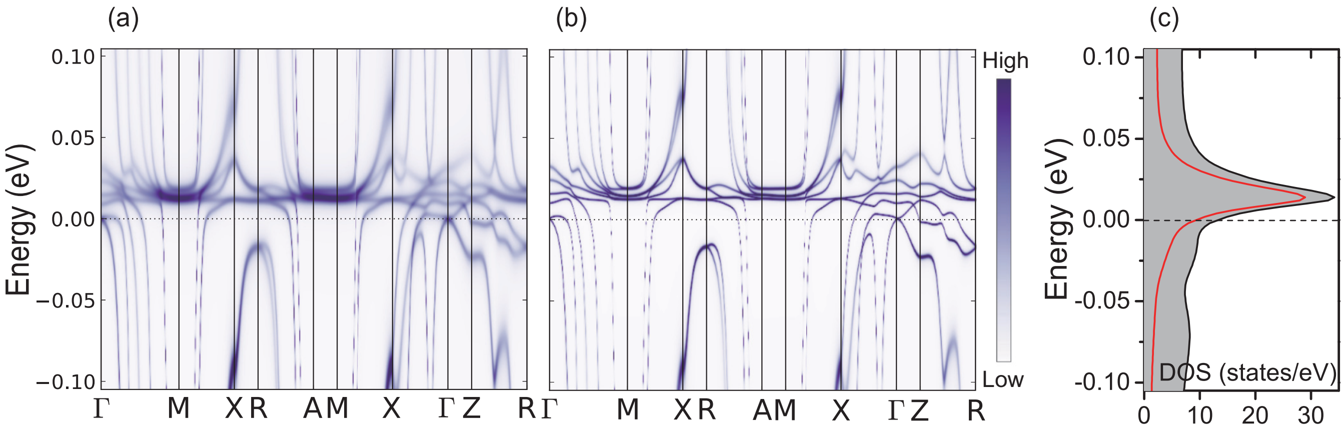

FIG. 8. (a) DFT + DMFT momentum-resolved spectral function of $CePt_2Si_2$ near Fermi energy at 10 K. (b) Modify $\mathrm{Im}\,\Sigma_{5/2}(\omega)$ to identify the low-lying hybridization bands and their crossings more clearly (see text). (c) DFT + DMFT DOS at 10 K, in which the black line denotes total DOS, red line shows DOS of $4f_{5/2}$ state.

Fig. 8(a), in which the band structure is similar to the DFT bands in Figs. 7(a) and 7(d), which treat Ce-$4f$ electrons to be itinerant. The hybridization bands of f-itinerant DFT also split into $4f_{5/2}$ and $4f_{7/2}$ bands by an energy interval close to that of DFT + DMFT. As shown in Fig. 7(b), the $4f$ DOS shows three major differences between DFT and DFT + DMFT results, firstly, the $4f$ peak width (198 meV in DFT) is strongly reduced to 20 meV in DFT + DMFT under electron correlations, with a reduction factor of 9.9 close to the mass enhancement $m^*/m_{\mathrm{DFT}} = 10.3$ in Eq. (3); secondly, in DFT + DMFT result, the $4f_{5/2}$ DOS shifts towards the Fermi level, forming Kondo resonance peak very close to the Fermi energy, while the DFT $4f_{5/2}$ DOS peak locates considerable higher above the Fermi level; thirdly, DFT + DMFT produces additional lower and upper Hubbard bands far away from the Fermi level.

In the literature, it has been shown that the nonsymmorphic symmetries combining point group with fractional translation operations can generate additional degeneracy along certain high-symmetry paths in the Brillouin zone, which are robust under action of SOC [9]. In space group No. 129, the nonsymmorphic symmetries are the gliding mirror plane $\{M_z|\frac{1}{2},\frac{1}{2}\}$ and screw axes $\{C_{2x}|\frac{1}{2},0\}$, $\{C_{2y}|0,\frac{1}{2}\}$, which are hold by $CePt_2Si_2$ and $CePt_2Ge_2$ crystals in Fig. 1(b). At $T > T_{\mathrm{KS}}$, since Ce-$4f$ electrons are already localized, the electron bands of $CePt_2Si_2$ can be reflected by $4f$ open-core DFT results in Fig. 7(c). With time-reversal symmetry in their paramagnetic phases, the space inversion symmetry of $CePt_2Si_2$ and $CePt_2Ge_2$ guarantees global twofold degeneracy of the electron bands, and the nonsymmorphic symmetries give additional degeneracy of bands at X, R, M, A points, therefore, fourfold Dirac crossings arise, generating Dirac nodes at these points. Moreover, degeneracy of bands remain along X-R and M-A paths [see Fig. 7(c)], resulting in DNLs, similar to ZrSiS and $PtPb_4$ [5–8]. The X-R and M-A DNLs locate at the boundary of the Brillouin zone, as shown in Fig. 1(c). The energy ranges of the X-R DNL in $CePt_2Si_2$ are (–0.725 eV, –0.624 eV) and (6.4 meV, 0.759 eV) from the Fermi level, while for M-A DNL it is in (–0.338 eV, –0.330 eV). At $T > T_{\mathrm{KS}}$, the similarity between spectral function [Fig. 6(e)] and $4f$ open-core bands in Fig. 7(c) clearly verifies above analyses of band crossings and appearance of DNLs in $CePt_2Si_2$ in local-moment region. It should be stressed that since the Ce-$4f$ electrons are already localized at $T > T_{\mathrm{KS}}$, such DNLs are noninteracting and are composed by light conduction electrons (mostly Ce-d, Pt-p, d, and Si-p electrons).

We have shown in Figs. 6(f) and 8(a) that below $T_{\mathrm{coh}} \approx 80\,\mathrm{K}$, the hybridization bands can be clearly identified near the Fermi level, in which their crossings at X, R and along X-R path are already legible, while at M, A and along M-A path seem a little fuzzy because several crossings concentrate in a narrow energy range. In order to see the DNLs more clearly, we slightly reduce the value of Σ_0 in the parabolic expression of imaginary self-energy $\mathrm{Im}\,\Sigma_{5/2}(\omega)$ and recalculate the spectral function. The obtained spectral function is displayed in Fig. 8(b), in which the locations of crossings between hybridization bands match f-itinerant DFT results in Fig. 7(d), confirming the existence of interacting DNLs along X-R and M-A paths, since such crossings are protected by lattice nonsymmorphic symmetries and robust under electron correlations. Nevertheless, below T_{coh}, electron correlations push the hybridization bands much closer to the Fermi level than f-itinerant DFT results, hence generate much narrow energy windows for X-R and M-A DNLs, which are about (–90 meV, –15 meV) and (12.5 meV, 37 meV) along X-R, and (12.5 meV, 18.8 meV) along M-A, from the Fermi level. Comparing Figs. 8(a) and 8(c), it can be seen that the energy window of M-A DNL locates at the center of the Kondo resonance peak; therefore, the Dirac fermions near M-A DNL are highly renormalized and are essentially the heavy-fermions hybridizing $4f_{5/2}$ electrons with conduction electrons. The energy window of X-R DNL locates at the lower tail of the Kondo resonance peak, thus the Dirac fermions near X-R DNL are also interacting.

From above discussions, we can now verify the appearance of interacting DNLs in $CePt_2Si_2$, locating along X-R and M-A paths in its Brillouin zone, driven by Kondo coherence below coherent temperature $T_{\mathrm{coh}} \approx 80\,\mathrm{K}$, and the energy windows of these DNLs are very close to the Fermi level. The Dirac fermions of these interacting DNLs are constructed by heavy-fermions with strongly enhanced effective mass and reduced velocity. As temperature rises from T_{coh}, the interacting DNLs

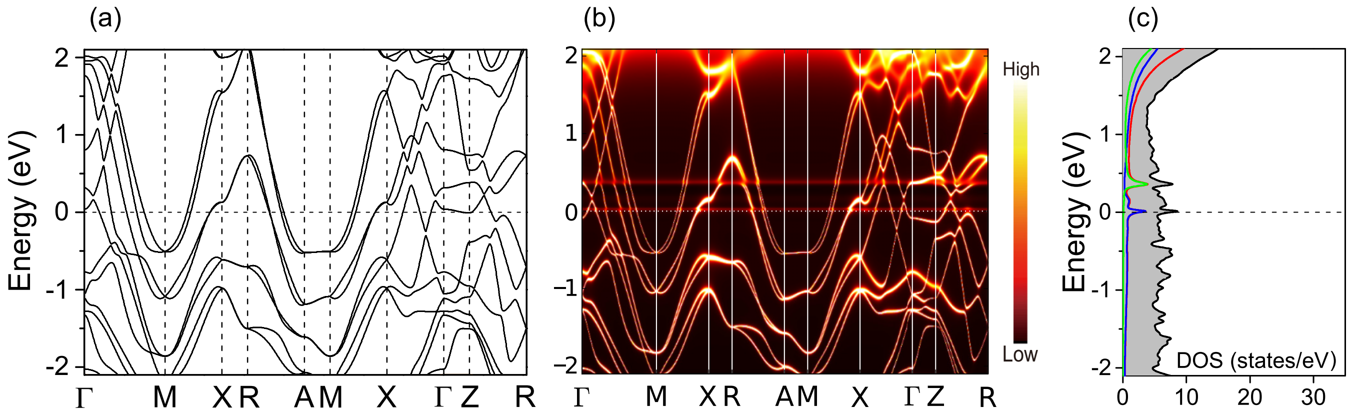

FIG. 9. (a) $4f$ open-core DFT bands of $\mathrm{CePt_2Ge_2}$ and (b) the momentum-resolved spectral function at 10 K via DFT + DMFT calculation. (c) Projected DOS by DFT + DMFT simulation at 10 K, in which the dashed horizontal line represents the Fermi level, black-solid line denotes total DOS, red line denotes Ce-$4f$ DOS, blue and green lines show projected Ce-$4f_{5/2}$ and $4f_{7/2}$ DOS, respectively.

are destructed gradually and are no longer clearly identified. Above the local Kondo screening temperature $T_{\mathrm{KS}} \approx 600\,\mathrm{K}$, the DNLs reappear near the Fermi level, but now the correlated $4f$ electrons are already localized, so now the Dirac fermions are composed of noncorrelated light conduction electrons. Besides, the energy ranges of the DNLs in these two cases are shifted dramatically, in that the energies of the noninteracting DNLs are much far from the Fermi level than the interacting DNLs.

Now we turn to discuss $\mathrm{CePt_2Ge_2}$. By contrast, the transition to Kondo-coherent state upon cooling in $\mathrm{CePt_2Si_2}$ does not emerge in $\mathrm{CePt_2Ge_2}$. In Fig. 9, we compare $4f$ open-core DFT bands with DFT + DMFT momentum-resolved spectral function at 10 K for $\mathrm{CePt_2Ge_2}$, which shows good correspondence. Even at such low temperature, the Ce-$4f$ states just contribute a small DOS near the Fermi level, and the $4f$ peak height is much smaller than that of $\mathrm{CePt_2Si_2}$ at low temperature. Besides, at 10 K, the imaginary $4f_{5/2}$ self-energy of $\mathrm{CePt_2Ge_2}$ has very large value at $\omega = 0$, similar to CeSb and γ-Ce, which are in local-moment region. Therefore, the $4f$ electrons are localized, suggesting the local-moment nature of Ce-$4f$ states in $\mathrm{CePt_2Ge_2}$, which can be directly verified by the similarity of $4f$ open-core DFT bands with the spectral function in Fig. 9. The strong suppression of Ce-$4f$ resonance peak in $\mathrm{CePt_2Ge_2}$ mainly results from about 7% volume increase of the unit cell than $\mathrm{CePt_2Si_2}$, which also drives the itinerant-localized shift of f electrons in $\alpha - \gamma$ phase transition of Ce metal [23]. Since the correlated $4f$ electrons are localized, the X-R and M-A DNLs in $\mathrm{CePt_2Ge_2}$ are noninteracting, and their energy ranges are (–0.708 eV, –0.615 eV) and (0.129 eV, 0.731 eV) for X-R, and (–0.521 eV, –0.507 eV) for M-A, all relatively far from the Fermi level. Similar to $\mathrm{CeIn_3}$ [20], contraction of the unit cell in pressured $\mathrm{CePt_2Ge_2}$ will significantly enhance the Kondo resonance peak at low temperature, and start to form clear heavy-fermion bands and interacting DNLs above certain pressure.

V. DISCUSSION AND CONCLUSIONS

To summarize, we have performed systematic DFT + DMFT simulations of $\mathrm{CePt_2Si_2}$ and $\mathrm{CePt_2Ge_2}$ in a wide temperature range. By examining the temperature dependence of Ce-$4f$ self-energies, Kondo resonance peak, magnetic susceptibility, and momentum-resolved spectral function for $\mathrm{CePt_2Si_2}$, we have verified a crossover from localization of Ce-$4f$ electrons to local Kondo screening of $4f$ electrons by *spd* conduction electrons, at Kondo screening temperature $T_{\mathrm{KS}} \approx 600\,\mathrm{K}$ upon cooling. Secondly, as temperature decreases further, a transition takes place from local Kondo screening to Kondo coherent state in $\mathrm{CePt_2Si_2}$ at coherence temperature $T_{\mathrm{coh}} \approx 80\,\mathrm{K}$, and the Kondo coherence is driven by indirect RKKY interaction between $4f$ electrons. In contrast, due to larger unit-cell volume than $\mathrm{CePt_2Si_2}$, Ce-$4f$ electrons in $\mathrm{CePt_2Ge_2}$ remain localized as low as 10 K.

The lattice nonsymmorphic symmetries in $\mathrm{CePt_2Si_2}$ and $\mathrm{CePt_2Ge_2}$ give rise to symmetry-protected DNLs along X-R and M-A high-symmetry paths in the Brillouin zone, which are robust under action of SOC and electron correlations. For $\mathrm{CePt_2Si_2}$, above T_{KS}, the local-moment nature of Ce-$4f$ electrons makes these DNLs noninteracting, mainly composing of light *spd* conduction electrons, and the energy windows of these DNLs are relatively far from the Fermi level. Below T_{coh}, the emergence of Kondo coherence drives the DNLs in $\mathrm{CePt_2Si_2}$ strongly interacting and constructing by heavy-fermions with strongly enhanced effective mass and reduced velocity. Remarkably, the energy range of the interacting DNLs is shifted to be much closer to the Fermi level. In intermediate temperature range $T_{\mathrm{coh}} < T < T_{\mathrm{KS}}$, the DNLs are no longer well identified. By contrast, in $\mathrm{CePt_2Ge_2}$, the DNLs along X-R and M-A paths are noninteracting in wide temperature region, consisting of only light conduction electrons.

It is well known that in some rare-earth semimetallic compounds, Weyl fermions can arise due to breaking of time-reversal symmetry by magnetic order, such as in Weyl node-point semimetals CeSb [26,31,32], CeBi [33,34], CeAlGe, CeAlSi and LaAlSi [35–38]; or arise by breaking of space-inversion symmetry in noncentrosymmetric lattices, such as in Weyl node-point semimetal $\mathrm{CeRu_4Sn_6}$ [39], and Weyl node-ring semimetals $\mathrm{Ce_3Bi_4Pt_3}$ [10,11] and YbCdGe [40]. In addition, Dirac fermions also emerge in node-line

Dirac semimetals CeRhSb and CeNiSn with centrosymmetric structures [14]. Although model studies have implied that heavy-Weyl or heavy-Dirac quasiparticles can emerge in Anderson lattice model [41,42], their appearance in real materials are rare. In most of above materials (except for Weyl semimetals $\mathrm{CeRu_4Sn_6}$ and $\mathrm{Ce_3Bi_4Pt_3}$), the f electrons in rare-earth atoms are actually localized, so the Weyl or Dirac fermions in these materials are composed of noninteracting conduction electrons. It should be also stressed that nonsymmorphic CeSbTe also holds DNLs in its paramagnetic phase; however, CeSbTe shows a magnetic order below 2.7 K, and the Ce-4f states are essentially localized in its paramagnetic phase [43], so their DNLs are formed by conduction electrons in all temperature region. In this context, our revealed interacting DNLs in $\mathrm{CePt_2Si_2}$ provides a very rare case of interacting Dirac fermions in real materials, besides, the dramatic change of Dirac fermions on the DNLs at different temperature regions provides an unique platform for future experimental investigations.

The bulk DNLs and induced surface states have been observed by ARPES experiments in nonsymmorphic ZrSiS [5–7] and $\mathrm{PtPb_4}$ [8], which exhibit noninteracting DNLs on the boundaries of their Brillouin zones; likewise, the interacting DNLs we proposed in $\mathrm{CePt_2Si_2}$ also locate along high-symmetric X-R and M-A lines, making it easier to be observed experimentally, and the drastic temperature variation of dispersions near the DNLs can also be detected conveniently. We find that the surface states induced by DNLs in $\mathrm{CePt_2Si_2}$ depend sensitively on the cleavage plane of the crystal, hence it requires further experimental data to obtain detailed surface dispersions. Besides, the interacting DNLs below T_{coh} may give rise to heavy surface states, which are distinct to ordinary light surface states above T_{KS} [44].

According to model studies of Weyl Kondo semimetals, the interacting node points or node lines can give rise to unusual transport phenomena in comparison with noninteracting cases, e.g., the strong mass enhancement and velocity reduction of Weyl nodes produce a T^3 temperature dependence of specific heat [10], while the Weyl node line provides two-dimensional Weyl fermions in momentum space, hence contributes a T^2 dependence of specific heat [30]. Moreover, the electron correlations in topological semimetals can induce nonlinear-response phenomena such as giant spontaneous Hall effect, as observed in node-line Weyl semimetal $\mathrm{Ce_3Bi_4Pt_3}$ [12,13]. Similarly, the interacting DNLs in $\mathrm{CePt_2Si_2}$ may also induce anomalous nonlinear responses, which deserves further experimental and theoretical investigations.

ACKNOWLEDGMENTS

This work is supported by GuikeAD20159009, National Natural Science Foundation of China (Grants No. 12004048, No. 11864008, and No. 11764010), the National Key Research and Development Program of China (Grant No. 2021YFB3501503), and the Foundation of LCP.

[1] Z. Wang, Y. Sun, X.-Q. Chen, C. Franchini, G. Xu, H. Weng, X. Dai, and Z. Fang, Phys. Rev. B **85**, 195320 (2012).

[2] Z. Wang, H. Weng, Q. Wu, X. Dai, and Z. Fang, Phys. Rev. B **88**, 125427 (2013).

[3] B. Q. Lv, H. M. Weng, B. B. Fu, X. P. Wang, H. Miao, J. Ma, P. Richard, X. C. Huang, L. X. Zhao, G. F. Chen, Z. Fang, X. Dai, T. Qian, and H. Ding, Phys. Rev. X **5**, 031013 (2015).

[4] Z. Wang, K. Luo, J. Zhao, and R. Yu, Phys. Rev. B **100**, 205117 (2019).

[5] B.-B. Fu, C.-J. Yi, T.-T. Zhang, M. Caputo, J.-Z. Ma, X. Gao, B. Q. Lv, L.-Y. Kong, Y.-B. Huang, M. Shi *et al.*, arXiv:1712.00782.

[6] L. M. Schoop, M. N. Ali, C. Straßer, A. Topp, A. Varykhalov, D. Marchenko, V. Duppel, S. S. P. Parkin, B. V. Lotsch, and C. R. Ast, Nat. Commun. **7**, 11696 (2015).

[7] C. Chen, X. Xu, J. Jiang, S.-C. Wu, Y. P. Qi, L. X. Yang, M. X. Wang, Y. Sun, N. B. M. Schröter, H. F. Yang, L. M. Schoop, Y. Y. Lv, J. Zhou, Y. B. Chen, S. H. Yao, M. H. Lu, Y. F. Chen, C. Felser, B. H. Yan, Z. K. Liu *et al.*, Phys. Rev. B **95**, 125126 (2017).

[8] H. Wu, A. M. Hallas, X. Cai, J. Huang, J. S. Oh, V. Loganathan, A. Weiland, G. T. McCandless, J. Y. Chan, S.-K. Mo *et al.*, npj Quantum Mater. **7**, 31 (2022).

[9] S. M. Young and C. L. Kane, Phys. Rev. Lett. **115**, 126803 (2015).

[10] H.-H. Lai, S. E. Grefe, S. Paschen, and Q. Si, Proc. Natl. Acad. Sci. USA **115**, 93 (2018).

[11] C. Cao, G.-X. Zhi, and J.-X. Zhu, Phys. Rev. Lett. **124**, 166403 (2020).

[12] A. Kofuji, Y. Michishita, and R. Peters, Phys. Rev. B **104**, 085151 (2021).

[13] S. Dzsaber, X. Yan, M. Taupin, G. Eguchi, A. Prokofiev, T. Shiroka, P. Blaha, O. Rubel, S. E. Grefe, H.-H. Lai, Q. Si, and S. Paschen, Proc. Natl. Acad. Sci. USA **118**, e2013386118 (2021).

[14] T.-S. Nam, C.-J. Kang, D.-C. Ryu, J. Kim, H. Kim, K. Kim, and B. I. Min, Phys. Rev. B **99**, 125115 (2019).

[15] A. Dommann, F. Hulliger, H. R. Ott, and V. Gramlich, J. Less-Common Met. **110**, 331 (1985).

[16] P. Dalmas de Réotier, A. Yaouanc, R. Calemczuk, A. D. Huxley, C. Marcenat, P. Bonville, P. Lejay, P. C. M. Gubbens, and A. M. Mulders, Phys. Rev. B **55**, 2737 (1997).

[17] K. Haule, C.-H. Yee, and K. Kim, Phys. Rev. B **81**, 195107 (2010).

[18] P. Blaha, K. Schwarz, F. Tran, R. Laskowski, G. K. H. Madsen, and L. D. Marks, J. Chem. Phys. **152**, 074101 (2020).

[19] J. H. Shim, K. Haule, and G. Kotliar, Science **318**, 1615 (2007).

[20] H. Lu and L. Huang, Phys. Rev. B **94**, 075132 (2016).

[21] X.-G. Zhu, Y. Liu, Y.-W. Zhao, Y.-C. Wang, Y. Zhang, C. Lu, Y. Duan, D.-H. Xie, W. Feng, D. Jian *et al.*, npj Quantum Mater. **5**, 47 (2020).

[22] Y.-C. Wang, Y.-J. Xu, Y. Liu, X.-J. Han, X.-G. Zhu, Y.-f. Yang, Y. Bi, H.-F. Liu, and H.-F. Song, Phys. Rev. B **103**, 165140 (2021).

[23] Q. Y. Chen, W. Feng, D. H. Xie, X. C. Lai, X. G. Zhu, and L. Huang, Phys. Rev. B **97**, 155155 (2018).

[24] C. Ayache, J. Beille, E. Bonjour, R. Calemczuk, G. Creuzet, D. Gignoux, A. Najib, D. Schmitt, J. Voiron, and M. Zerguine, J. Magn. Magn. Mater. **63-64**, 329 (1987).

[25] M. B. Tchoula Tchokonté, P. de V. du Plessisb, and A. M. Strydom, Solid State Commun. **136**, 450 (2005).

[26] H. Lu and Q. Liu, J. Phys.: Condens. Matter **32**, 485601 (2020).

[27] M. B. Tchoula Tchokonté, P. de V. du Plessis, A. M. Strydom, and D. Kaczorowski, J. Magn. Magn. Mater. **226-230**, 173 (2001).

[28] T.-S. Nam, Junwon Kim, C.-J. Kang, Kyoo Kim, and B. I. Min, Phys. Rev. B **103**, 045101 (2021).

[29] S. Burdin, A. Georges, and D. R. Grempel, Phys. Rev. Lett. **85**, 1048 (2000).

[30] L. Chen, C. Setty, H. Hu, M. G. Vergniory, S. E. Grefe, L. Fischer, X. Yan, G. Eguchi, A. Prokofiev, S. Paschen, J. Cano, and Q. Si, Nat. Phys. **18**, 1341 (2022).

[31] C. Guo, C. Cao, M. Smidman, F. Wu, Y. Zhang, F. Steglich, F.-C. Zhang, and H. Yuan, npj Quantum Mater. **2**, 39 (2017).

[32] Y. Fang, F. Tang, Y. R. Ruan, J. M. Zhang, H. Zhang, H. Gu, W. Y. Zhao, Z. D. Han, W. Tian, B. Qian, X. F. Jiang, X. M. Zhang, and X. Ke, Phys. Rev. B **101**, 094424 (2020).

[33] S. Huan, X. Shi, L. Han, H. Su, X. Wang, Z. Zou, N. Yua, W. Zhao, L. Chene, and Y. Guo, J. Alloys Compd. **875**, 159993 (2021).

[34] C. E. Matt, Y. Liu, H. Pirie, N. C. Drucker, N. H. Jo, B. Kuthanazhi, Z. Huang, C. Lane, J.-X. Zhu, P. C. Canfield, and J. E. Hoffman, Phys. Rev. B **105**, 085134 (2022).

[35] G. Chang, B. Singh, S.-Y. Xu, G. Bian, S.-M. Huang, C.-H. Hsu, I. Belopolski, N. Alidoust, D. S. Sanchez, H. Zheng, H. Lu, X. Zhang, Y. Bian, T.-R. Chang, H.-T. Jeng, A. Bansil, H. Hsu, S. Jia, T. Neupert, H. Lin, and M. Z. Hasan, Phys. Rev. B **97**, 041104(R) (2018).

[36] P. Puphal, V. Pomjakushin, N. Kanazawa, V. Ukleev, D. J. Gawryluk, J. Ma, M. Naamneh, N. C. Plumb, L. Keller, R. Cubitt, E. Pomjakushina, and J. S. White, Phys. Rev. Lett. **124**, 017202 (2020).

[37] H. Su, X. Shi, J. Yuan, Y. Wan, E. Cheng, C. Xi, L. Pi, X. Wang, Z. Zou, N. Yu, W. Zhao, S. Li, and Y. Guo, Phys. Rev. B **103**, 165128 (2021).

[38] A. P. Sakhya, C.-Y. Huang, G. Dhakal, X.-J. Gao, S. Regmi, X. Yao, R. Smith, M. Sprague, B. Singh, H. Lin *et al.*, arXiv:2203.05440.

[39] Y. Xu, C. Yue, H. Weng, and X. Dai, Phys. Rev. X **7**, 011027 (2017).

[40] A. Laha, S. Malick, R. Singha, P. Mandal, P. Rambabu, V. Kanchana, and Z. Hossain, Phys. Rev. B **99**, 241102(R) (2019).

[41] S. E. Grefe, H.-H. Lai, S. Paschen, and Q. Si, Phys. Rev. B **101**, 075138 (2020).

[42] P.-Y. Chang and P. Coleman, Phys. Rev. B **97**, 155134 (2018).

[43] L. M. Schoop, A. Topp, J. Lippmann, F. Orlandi, L. Müchler, M. G. Vergniory, Y. Sun, A. W. Rost, V. Duppel, M. Krivenkov *et al.*, Sci. Adv. **4**, eaar2317 (2018).

[44] R. Peters, T. Yoshida, H. Sakakibara, and N. Kawakami, Phys. Rev. B **93**, 235159 (2016).